1   **Electronic Supplementary information (ESI)** *for*

2

3   **Lithiation induced crystal restructure of hydrothermal**

4   **prepared Sn/TiO$_2$ nanocrystallite with substantial enhanced**

5   **the capacity and cycling performance for lithium-ion battery**

6

7   *Tsan-Yao Chen[a,b]*, Yu-Ting Liu[c] ,Ping-Ching Wu[d] ,Chih-Wei Hu[a] ,Po-Wei Yang[a] ,*

8   *Liang-Ching Hsu[c] , Chih-Hao Lee[a] , and Chia-Chin Chang[d]**

9

10   Affiliations:

11   *[a] Department of Engineering and System Science, National Tsing Hua University,*

12   *Hsinchu 30013, Taiwan*

13   *[b] Institute of Nuclear Engineering and Science, National Tsing Hua University,*

14   *Hsinchu 30013, Taiwan*

15   *[c] Department of Soil and Environmental Science, National Chung Hsing University,*

16   *Taichung 402, Taiwan*

17   *[d] Department of Greenergy Technology, National University of Tainan, Tainan 7005,*

18   *Taiwan*

19   [*]To whom correspondence should be addressed:

20   Chia-Chin Chang, email: ccchang@mail.nutn.edu.tw ; Tel: +886-6-268-9274 (O);

21   +886-6-260-2205 (Fax)

22

1. Microstructure of Sn doped TiO_2 (2ST) and TiO_2

The lattice slices for 2 x 2 slabs of (101) facet of TiO_2-A and (110) facet of TiO_2-R are shown in Fig. S1. As shown in Fig. S1a, the topmost layer of TiO_2-A (101) facet comprising all Ti atoms with the symmetry of P2. The interatomic distances between center and Ti atoms at two edge axis are determined to be 5.730 and 5.376 Å with the interatomic cross angle of 69.703° / 110.297°, respectively. On the other hand, the topmost layer of TiO_2 (110) facet comprising Ti and O atoms in the symmetry of Cmm2. In this slice, the interatomic distances between Ti and O atoms are determined to be 1.936 / 1.960 Å with the cross angle of 80.913° / 99.087°.
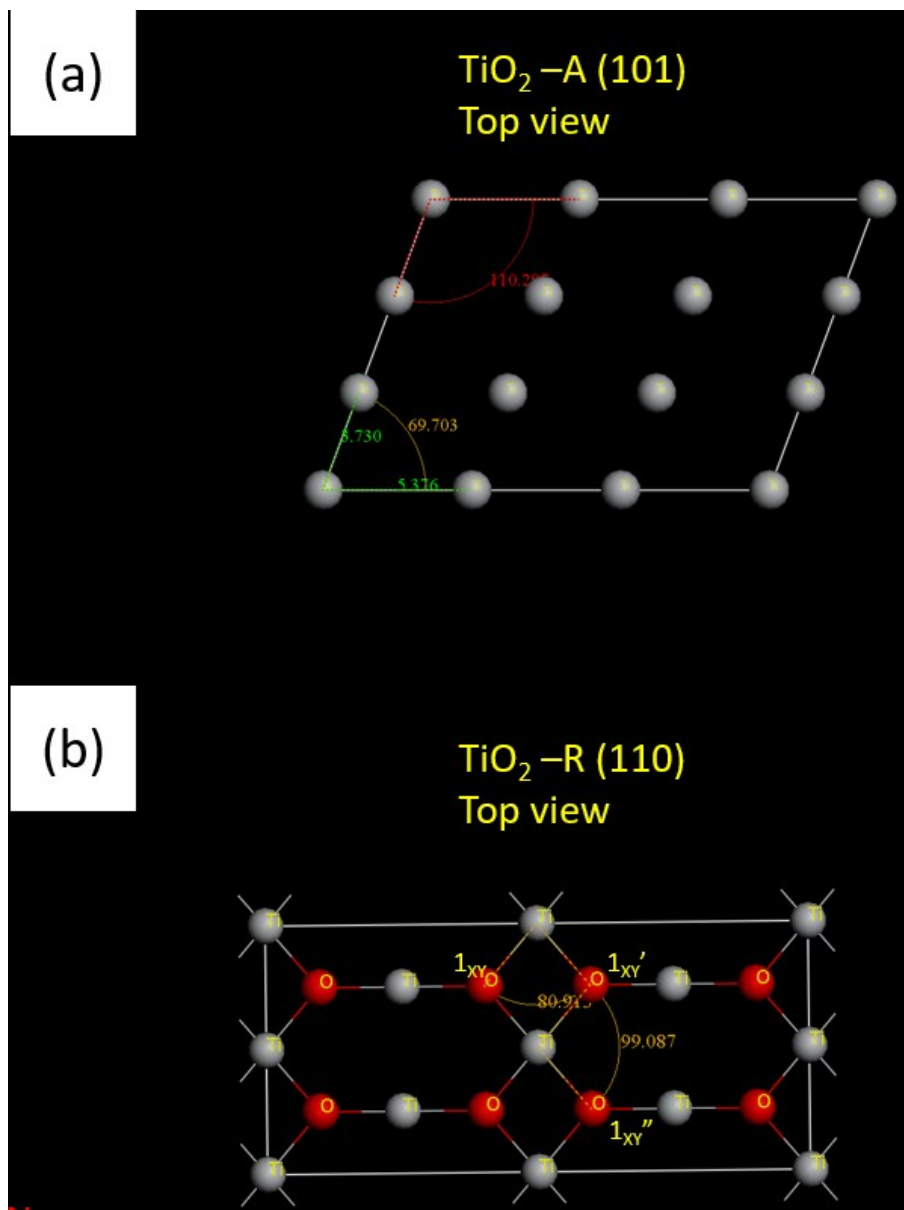
Fig. S1. The lattice slices for (a) (101) facet of TiO_2-A and (b) (110) facet of TiO_2-R.

36   The microstructure of the experimental negative electrodes were illustrated by
37 scanning electron microscopy and transmission electron microscopy. As can be seen,
38 there are segregated nanoparticles (in an average size of 3 – 4 nm) segregating at the
39 surface of rectangular crystallites (in a size ranging from 100 to 120 nm). Such results
40 consistently prove the finding of XRD indicating that the surface segregation of SnO_2
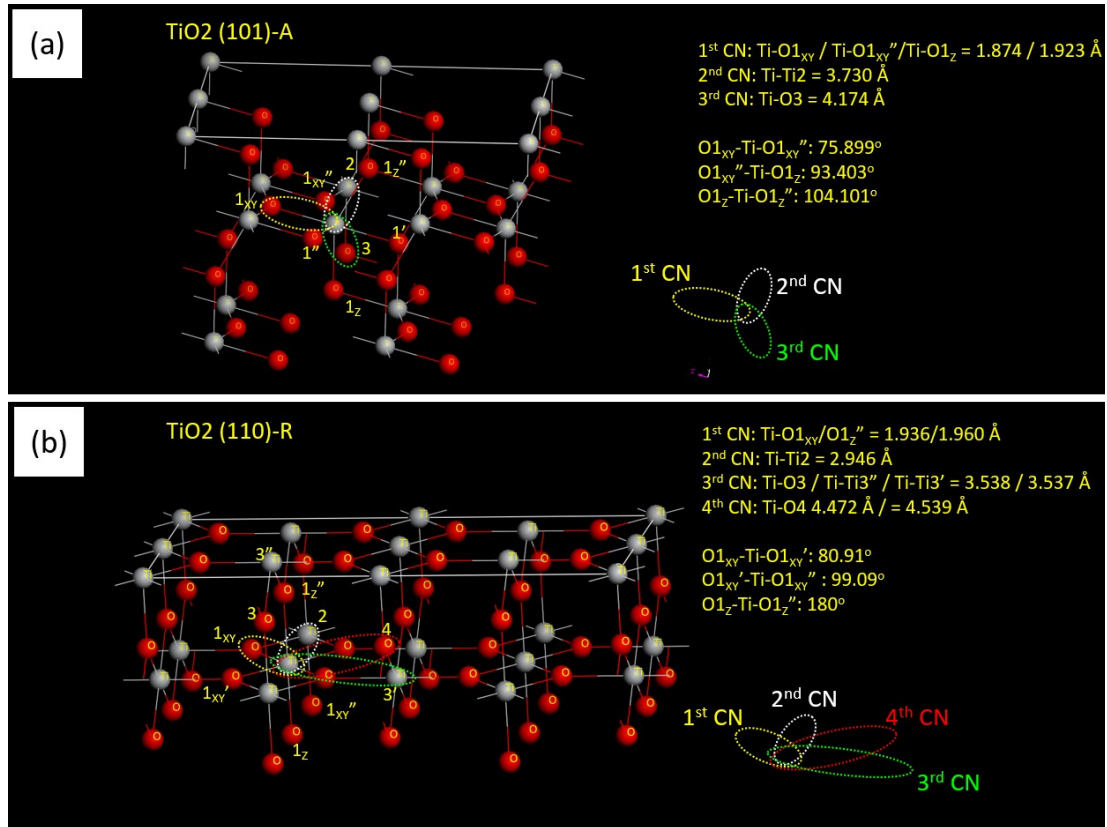41 at $SnTiO_2$. The results of EDX are given in **Table S1**.
42
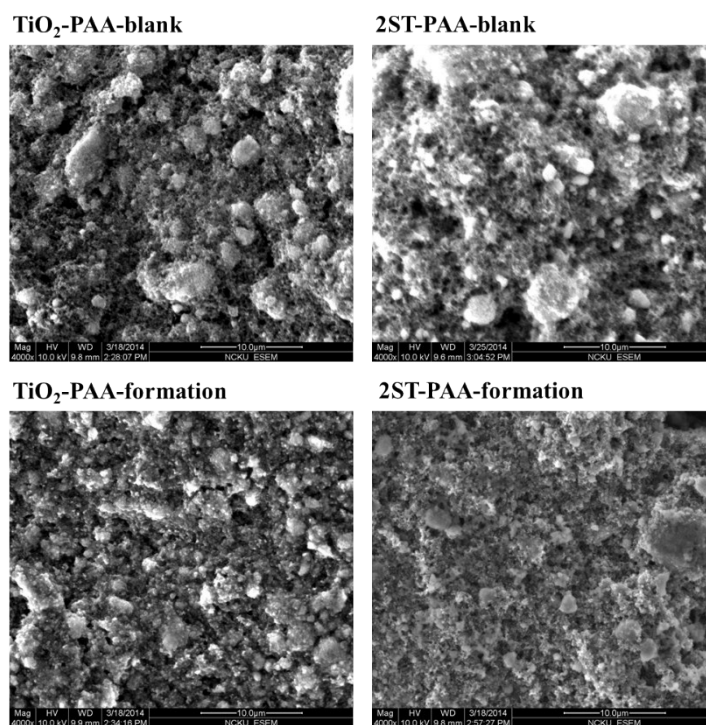
43

44 **Fig. S2** The scanning electron microscopy images of TiO_2 and 2ST electrode (with
45 the binder of PAA) before (blank) and after (formation) LIB formation.
46
47   **Table S1**. The EDX results of 2ST sample

| element	atomic ratio (%)
Ti	82.4
Sn	17.6

48
49

Fig. S3 Atomic structure model for the (a) (101) facet of TiO_2-A and (b) (110) facet of TiO_2-R.

The atomic structure model for the (101) facet of TiO_2-A and (110) facet of TiO_2-R are shown in Fig. S3a and S3b, respectively. Accordingly, there are three coordination shells including 1st CN for Ti-O1$_{XY}$ / TiO1XY" / TiO1Z with the distance of 1.874 / 1.874 / 1.923 Å; 2nd CN for Ti-Ti2 with the distance of 3.730 Å; 3rd CN for Ti-O3 with the distance of 4.174 Å. The cross angles between O1$_{XY}$-Ti-O1$_{XY}$", O1$_{XY}$-Ti-O1$_{Z}$, and O1$_{Z}$-Ti-O1$_{Z}$" are determined to be 75.899, 93.403, and 104.101°, respectively. For the case of TiO_2-R (110), the local structure in the first four CN shell are Ti-O1$_{XY}$/Ti-O1$_{Z}$", Ti-Ti2, Ti-O3, Ti-Ti3, and Ti-O4, respectively. In this facet, the cross angles of O1$_{XY}$-Ti-O1$_{XY}$', O1$_{XY}$'-Ti-O1$_{XY}$", and O1$_{Z}$-Ti-O1$_{Z}$" are determined to be 80.91, 99.09, and 180o, respectively. These structure information

63 consistently proved the contribution of radial structure peaks in the Ti K-edge EXAFS
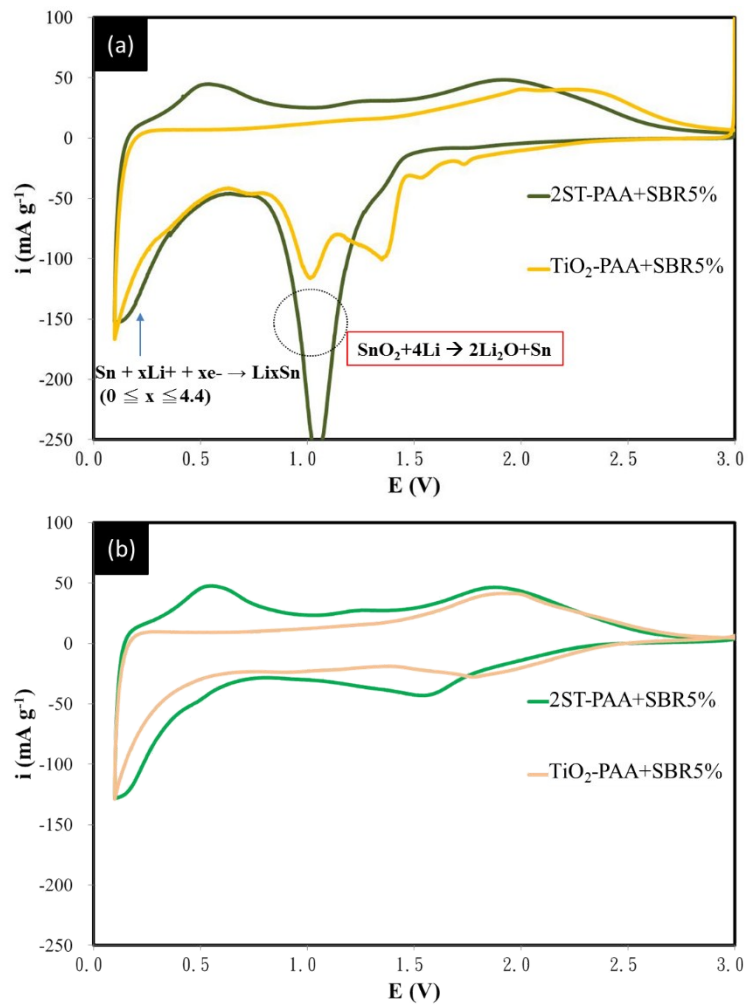
64 spectra of experimental samples Fig. 3.

65
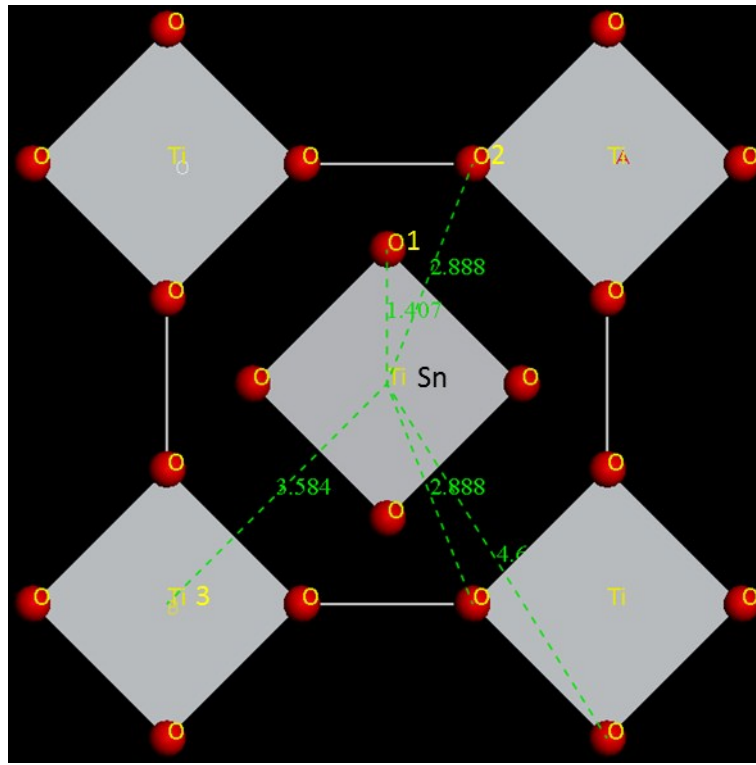
Fig. S4. The crystal structure with interatomic bond length at the first three coordination shells (Ti/Sn-O1, Ti/Sn-O2, Ti/Sn-Ti3) of $Sn_{0.1}Ti_{0.9}O_2$

68

69 *2. Cyclic voltammetry analysis on the negative electrodes of TiO$_2$ and 2ST in LIB*

70 *cell*

71 The Cyclic voltammetry sweeping curves of 2ST and TiO$_2$ powder mixed with 5

72 wt% of conducting carbon (SBR) and binder (PAA) in negative electrode at the 1st

73 and 2nd CV sweeping curve are shown in Fig. S5a and S5b, respectively, with the

74 voltage scan ranging from 0 to 3.0 volts. In S3a, as clearly shown, there are several

75 reaction peaks at the 2.0 to 0.8 volts on the 1st CV sweeping curve of TiO$_2$. These

76 peaks can be attributed to the formation of surface chelation reaction between the

77 ligands of binder (PAA) and the OH- sites at different sorption sites of the TiO$_2$

78 surface. For the case of 2ST, the reaction peaks across 1.8 − 0.8 volts shall correspond

79 to the contributions of surface binder chelation as that were found on TiO$_2$. Here, a

80 substantial enhanced peak is found at 1.3 − 0.8 volts and can be attributed to the

81 formation of Li$_2$O by interacting the Li ions with the SnO$_2$ (**SnO$_2$ + 4Li$^+$ + 4e$^-$ →**

82 **2Li$_2$O + Sn**) with the subsequent formation of SnLix (**Sn + xLi$^+$ + xe$^-$ → Li$_x$Sn, 0 ≦**

83 **x ≦ 4.4)** at the low voltage range (0.4 − 0.0 volts). These features reveals the

84 presence of Li$_x$Sn local alloying and the presence of surface SnO$_2$ residuals on the

85 freshly prepared 2ST powders. In **Fig. S5b**, the absence of surface chelation and SnO$_2$

86 reduction peaks indicate that the completeness of SnO$_2$ reduction and formation of

87 Li$_x$Sn in the 1st CV cycle.

(a) curve with annotations:

$Sn + xLi+ + xe- \rightarrow LixSn$
$(0 \leqq x \leqq 4.4)$

$SnO_2 + 4Li \rightarrow 2Li_2O + Sn$

2ST-PAA+SBR5%

TiO_2-PAA+SBR5%

(b) curve:

2ST-PAA+SBR5%

TiO_2-PAA+SBR5%
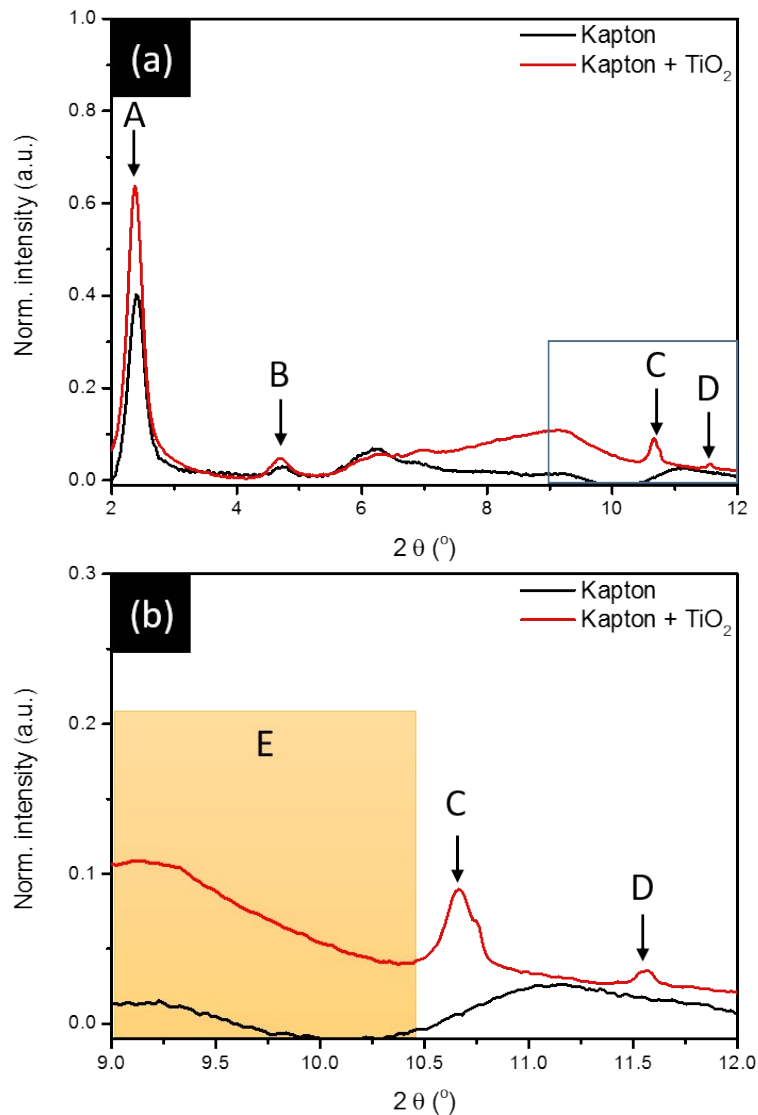
Fig. S5. The cyclic voltammetry sweeping curves of 2ST and TiO_2 negative electrode mixing with 5 wt% of conducting carbon (SP) and binder (PAA) at (a) 1st and (b) 2nd CV cycles.

3. XRD analysis for X-ray window of coin cell "Kapton (polyimide)"

96

Fig. S6a XRD patterns of Kapton and Kapton coated with TiO_2 thin film; (b) inset of Fig. S6a (ref: https://wiki-ext.aps.anl.gov/ug11bm/index.php/Supplies_and_Tools)

The XRD pattern of Kapton was compared with that of Kapton coated with TiO_2 thin film in Fig. S6a and S6b. The peaks A and B denote the diffraction lines of kapton film at d spaces of 15.78 and 6.93 Å, respectively. The peaks C and D denote the diffraction lines of (101) and (110) facets for TiO_2-A and TiO_2-R, respectively. In the spectrum of Kapton + TiO_2 (Fig. S6b), the background was lifted by the diffusion scattering from the binder and conducting carbon additives in the TiO_2 thin film.
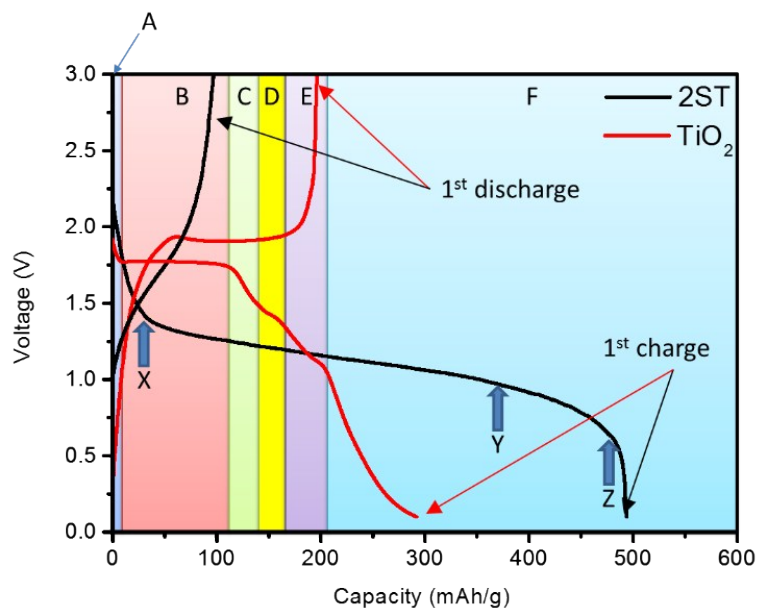
106 Accordingly, no diffraction peaks appear from 9 to 12° on spectrum of Kapton thin

107 film. It means that, the spectrum features of the negative electrode material in in-situ

108 experiments were not affected by the diffraction or scattering signals from the Kapton

109 window.

110

111

112 *4. Electrochemical performance of experimental LIB*

113

114 **Fig. S7** Charge / Discharge (lithiation / delithiation) curves of LIB coin cell with TiO_2
115 and 2ST negative electrode during *in-situ* XRD analysis. The current density is set to
116 be 0.03 mA mg^{-1} with the charge/discharge potential from 0.1 to 3.0 V. The
117 experimental coin cells were assembled and aged for 3 days prior to the in-situ XRD
118 measurements.

119

120   Fig. S7 shows the charge / discharge (Li insertion / extraction) characteristic

121 curve (C-E curve) of LIB with TiO_2 and 2ST negative electrode in formation cycle.

122 The six regions A, B, C, D, E and F (with different Capacity to Voltage slopes) can be

123 assigned to the features of Li$^+$ insertion at different chemical (potential) stages of

124 TiO_2 in LIB. In region A (from 3.0 to 1.75 volt), the voltage drop can be attributed to

125 the formation of Li insertion site at TiO_2-R surface. By applying voltage higher than

126 1.75 volt, a plateau from 10 to 110 mAhg^{-1} (region B) is the typical feature for the Li$^+$

127 intercalation to ion channel of TiO_2-R. By increasing capacity from 120 to 210 mAhg^{-1}

128 ^{1}, the slides in regions C (1.75 - 1.52 volt), D (1.52 - 1.41 volt), and E (1.41 - 1.10 volt)

129 were caused by the intercalation of Li^+ into the vacancy sites of distorted TiO_2-A at

130 the core-shell interface, the formation of Li^+ insertion site at TiO_2-A surface, and the

131 extrusion of Li^+ to the TiO_2-A core crystallite. By increasing capacity higher than 210

132 mAhg^{-1} (region F), the dramatic voltage drop reveals the suppression of further Li

133 insertion by the closed pore diffusion barrier at TiO_2-A core. In this case, the

134 formation of Li^+ pillows consumes certain cell potential and thus results in the

135 gradient distribution in the region F. Upon discharging, the C-E curve shows the

136 typical profile with a gradient of Li^+ diffusion; where a large irreversibility of

137 capacity is found between charge (300 mAhg^{-1}) and discharge (200 mAhg^{-1}) state.

138 Only one discharge plateau is found from 180 to 60 mAhg^{-1} at 1.9 volt. By decreasing

139 the capacity less than 60 mAhg^{-1}, potential is dropped from 1.9 to 0.1 volt by

140 completely discharging the LIB. These are typical characters for C-E curves of TiO_2-

141 A and TiO_2-R as negative electrode in LIB. After the1st charge-discharge cycle, the

142 ion channels were aligned by the lattice relaxation at the core - shell interface,

143 therefore, resulting in the indistinct stage profile in the regions C to E of TiO_2 (Fig. S8)

144 in the 2nd and 3rd charge curves. These features prove the formation of pillow

145 (formation of Li_xTiO_2) at Li channels which play important role in the irreversibility

146 of TiO_2 as consistently proved by the *in-situ* XRD analysis (Fig. 4b).

147   For 2ST negative electrode in LIB, the cell voltage was dropped from 3.0 to 1.45

148 volte upon increasing the capacity to 35 mAhg^{-1} (denoted by arrow X). This voltage

149 drop is larger than that of TiO_2 negative electrode and can be attributed to the

150 formation of Li_2O and Sn metal (by $SnO_2 + 4Li+ + 4e^- \rightarrow 2Li_2O + Sn$ reaction at 1.5

151 to 0.8 V as shown in the CV curve of 2ST Fig. S5) by interactions between SnO_2 and

152 Li^+. By further charging the LIB to 360 mAhg^{-1}, a slight voltage drop (1.45 to 0.95

153 volt) was found between arrow X and arrow Y. According to *in-situ* XRD results (Fig.

154 4a), we notice the absence of diffraction lines from 2ST-P in the presence of TiO_2-R

155 (110) (peak G) and TiO_2-A (101) facets (peak E) simultaneously with the Li

156 intercalated TiO_2-R (110) (peak G_L) and TiO_2-A (101) facets (peak E_L) in *in-situ*

157 XRD patterns (Fig. 4) by increasing SOC larger than 5 till 85% (~450 mAhg^{-1}). The

158 progressive potential drop (from 0.85 to 0.71 volt) is caused by the phase transition

159 from $Sn_{0.1}Ti_{0.9}O_2$ to TiO_2-R and TiO_2-A by the lattice relaxation and Li^+ intercalation.

160 Further increasing the capacity till 495 mAhg^{-1} causing a dramatic voltage drop to 0.1

161 volt. This phenomenon can be assigned to the formation of local $SnLi_x$ alloy (as

162 consistently revealed by CV analysis in Fig. S5) thus resulting in its superior capacity

163 comparing to TiO_2. The irreversibility of 2ST was determined to be 80% (390 mAhg^{-1},

164 490 →100 mAhg^{-1}) which is 2.9-fold higher than that of TiO_2 (33.8%, 295→195

165 mAhg^{-1}). Such abnormal property seemly hindered the application of 2ST in LIB,

166 however, can be substantially improved by mixing proper amount of conducting

167 carbon (SP, 20 wt% relative to active materials in our cases). According to the C-E

168 curves of LIB with SP mixed negative electrodes, the irreversibility of TiO_2 (Fig. S8a)

169 and 2ST (Fig. S8b) negative electrodes at the charge and discharge states at the first

170 three CE cycles were reduced to 28/5/5% and 27/6/6%, respectively. It means that the

171 Li extraction of 2ST is efficiently facilitated by placing the conductive particles in

172 active material.

173

174
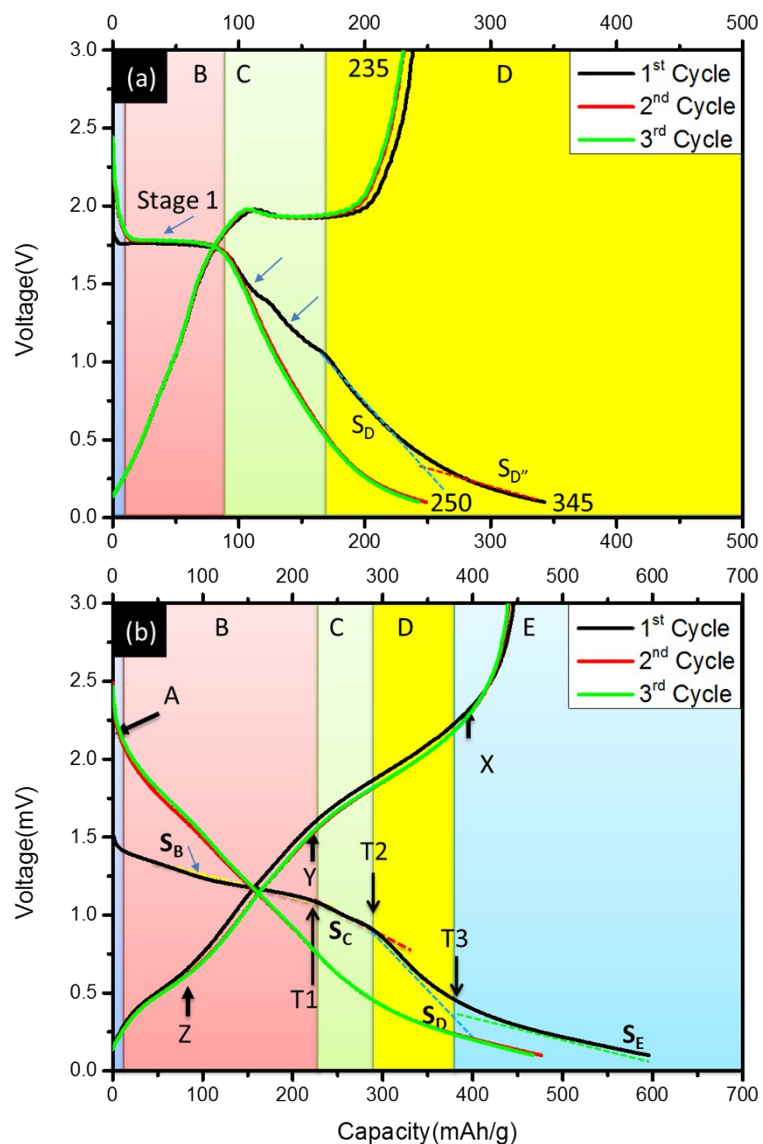
Fig. S8 Charge / Discharge (lithiation / delithiation) curves of LIB coin cell with TiO$_2$

and 2ST negative electrode during *in-situ* XRD analysis. The negative electrode was

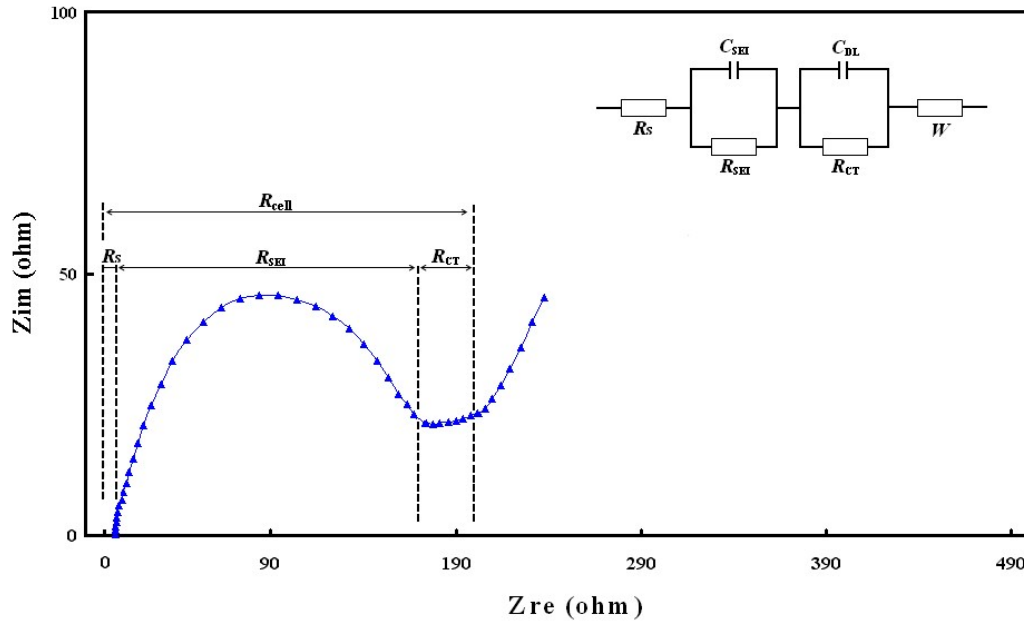prepared by mixing the experimental powders with the conductive carbon. The

current density is set to be 0.03 mA mg^{-1} with the charge/discharge potential from 0.1

to 3.0 V.

181 *5. Electrochemical impednace analysis of half cells containing experimental*

182 *negative electrodes*

183

184

185 Fig. S9. The proposed electrical equivalent circuit for modeling the EIS spectra of

186 experimental LIB.

187

188 Table S2. The model simulated electrochemical impedance parameters of half LIB

189 cell with (a) TiO_2 (TiO_2) and (b) $Sn_{0.1}Ti_{0.9}O_2$ (2ST-P) negative electrode materials.

190 The caption ended by -3D and -3DF denote the EIS spectra of negative electrode

191 before and after 1st charge / discharge cycle of LIB, respectively.

sample	Rs (W)	R_{SEI} (W)	R_{CT} (W)
TiO_2 -3D	8.61	120	700
TiO_2 -3DF	8.12	74.73	194.7
2ST-P-3D	10.82	59	97.6
2ST-P-3DF	5	15	73

192

193

6. XPS analysis

The XPS spectra of of Sn-TiO$_2$ samples (immersed in electrolyte for 1 hour (ST-1H), 3 days (ST-3DAY), and after LIB formation (ST-Formation)) at C 1s, O 1s, Sn 3d, and Ti 2p$_{3/2}$ orbitals were compared in Fig. S10. It clearly shown that the four elements (including Sn) were prevailing at particle surface in the sample immersed for 1 hour. As consistently revealed by result of EDX analysis, the XPS spectra proved the presence of Sn composition in the experimental sample. Increasing the immersion time or formation of LIB reduced the intensity of emission lines for metal elements with the substantially enhanced C1s and O1s peaks. These phenomenon reveals the formation of solid state interface atop the active materials.
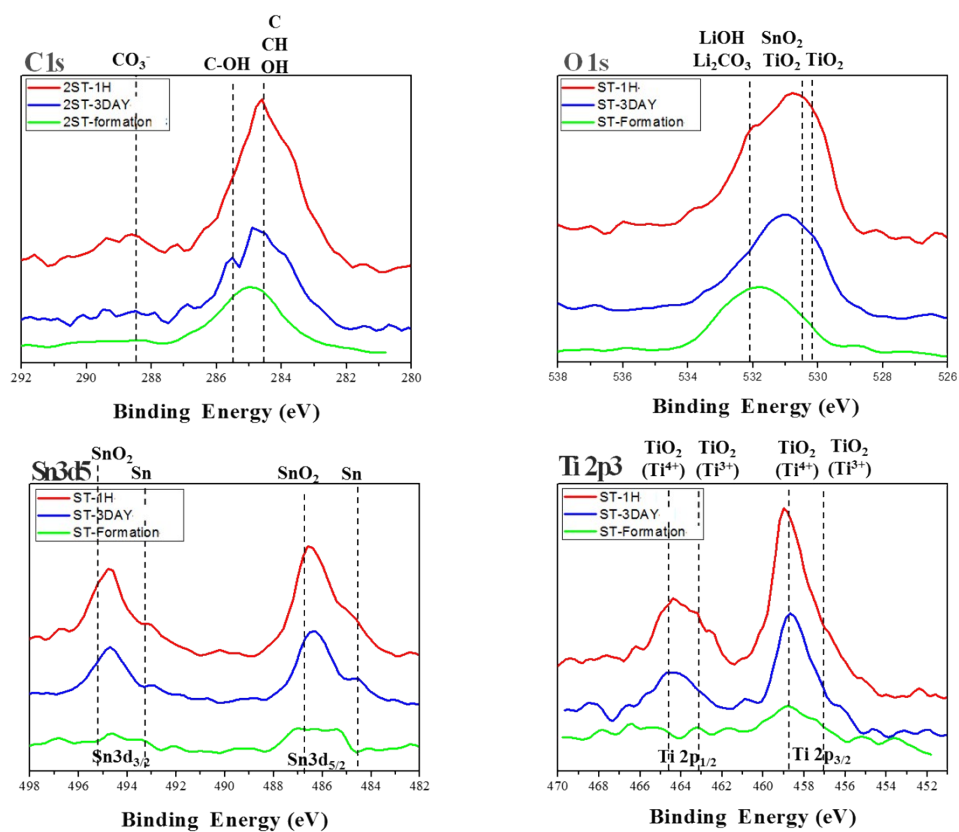
Fig. S10. The XPS spectra of Sn-TiO$_2$ samples at C 1s, O 1s, Sn 3d, and Ti 2p$_{3/2}$ orbitals.
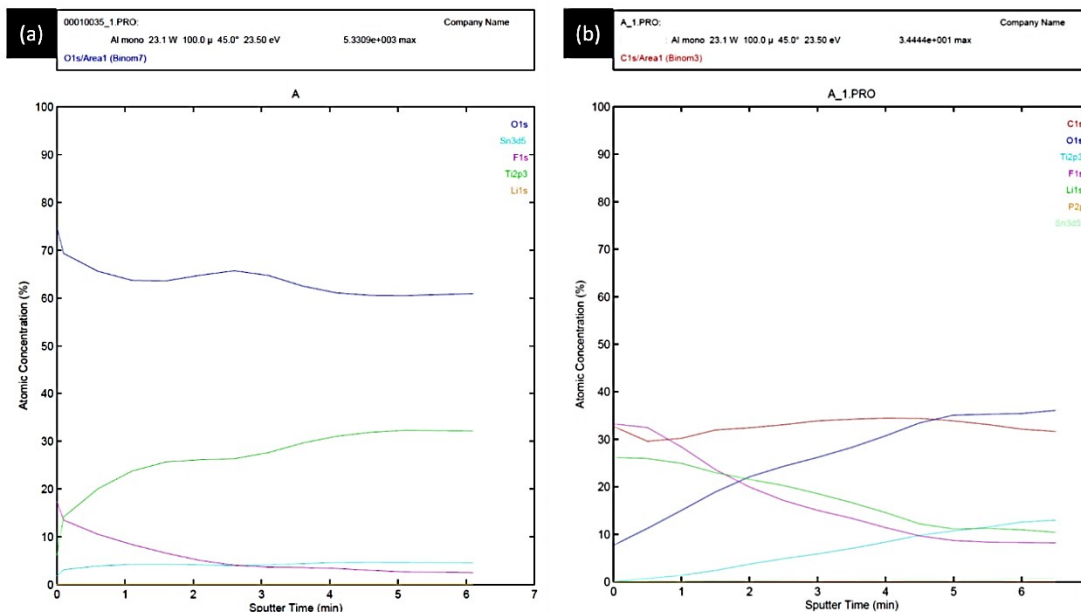
209

210 Fig. S11 The XPS depth profile of (a) freshly prepared 2ST-P electrode and (b) that

211 with 250 Charge – Discharge cycles.

212

213 　　　The depth profile of freshly prepared 2ST-P electrode and that with 250 Charge

214 – Discharge cycles were demonstrated in Fig. S11. The obtained results indicating the

215 presence of Sn at (Fig. 3a) 2ST-P and formation of SEI (as proved by high

216 composition of C at the sample surface. The concentration of Sn was determined to be

217 4 to 5 at% by increasing the sputter time from 0 to 6 hours at the sputtering rate of 3

218 nm per hour vs. Si wafer.